Asymmetric Butler-Volmer Kinetics of the Electrochemical Ce(III)/Ce(IV) Redox Couple on Polycrystalline Au Electrodes in Sulfuric Acid and the Dissociation Field Effect

Adrian Heinritz[1], Tobias Binninger[1,2,*,†], Alexandra Patru[1], and Thomas J. Schmidt[1,3]

[1] *Electrochemistry Laboratory, Paul Scherrer Institut, 5232 Villigen, Switzerland.*
[2] *ICGM, Univ Montpellier, CNRS, ENSCM, 34095 Montpellier, France.*
[3] *Laboratory of Physical Chemistry, ETH Zürich, 8093 Zürich, Switzerland.*

[*] *Corresponding author, Email: tobias.binninger.science@gmx.de*
[†] *Present address: ICGM, Univ Montpellier, CNRS, ENSCM, 34095 Montpellier, France.*

Abstract

The kinetics of the electrochemical Ce(III)/Ce(IV) redox couple in sulfuric acid on polycrystalline gold electrodes reveal an intriguing behavior. With an experimental approach to separately investigate the kinetics of Ce(III) oxidation and Ce(IV) reduction within the same potential range, we found perfect Butler-Volmer behavior with an extreme asymmetry: Accurate linear fits of the kinetic current Tafel plots yielded anodic and cathodic transfer coefficients of $\alpha_{anodic} = 0.84 \pm 0.02$ and $\alpha_{cathodic} = 0.157 \pm 0.006$, respectively, adding up to 1.00 ± 0.02, thus fulfilling the theoretical requirement of $\alpha_{anodic} = (1 - \alpha_{cathodic})$ at an experimentally unique precision. Several different flavors of Marcus theory could not reproduce the data with the same precision as the phenomenological asymmetric Butler-Volmer equation. Instead, our results suggest that the Ce(III)/Ce(IV) kinetics on gold electrodes in sulfuric acid are determined by a combination of the Frumkin effect and the field effect on the dissociation of cerium–sulfate complexes. The same mechanism could be responsible for a surprising enhancement of the Ce(IV) reduction kinetics observed during the reduction of an electrochemically pre-oxidized gold surface. Although the reaction proceeds in the outer (diffuse) part of the electrochemical double-layer, its kinetics are found to be sensitive to specific properties of the electrode material and surface, namely the potential of zero charge and the presence of surface adsorbates. Our findings could thus provide an example how electrocatalysis can act in the diffuse layer beyond the outer Helmholtz plane. The electrochemical Ce(III)/Ce(IV) redox couple on gold electrodes in sulfuric acid therefore represents a highly interesting model reaction for further development of fundamental electrocatalysis both from the experimental and theoretical perspective, with possible relevance, e.g., for redox flow battery development.

Keywords: electrocatalysis, cerium redox, Marcus theory, Frumkin effect, dissociation field effect, potential of zero charge, gold electrode, sulfate adsorption

Introduction

The cerium redox couple in solution has a versatile range of applications [1]. Being a strong oxidant, Ce(IV) is capable of completely oxidizing organic compounds to CO_2 in closed acidic systems, which has been successfully tested for waste water treatment in a pilot plant [2]. It is used in organic chemistry [3], where it serves as a redox mediator for a variety of reactions, and it is industrially relevant, e.g. for the oxidation of naphthalene to naphthoquinone at a 100-tons-per-year scale [1], and for the synthesis of vitamin K_3 at a 400-tons-per-year scale [1, 4]. It also proved to be suitable for gas scrubbing to remove harmful gases like H_2S, NO_x, and SO_2 [5], where gas removal efficiencies of 95%, 45%, and 100% were demonstrated, respectively [6]. Because of its numerous applications, recycling and regeneration of cerium, e.g. via electrochemical routes, becomes increasingly important for economic and ecological reasons. The urgent need to store electrical energy provided by intermittent renewable sources led to a strong current interest in redox flow batteries. Because of its high equilibrium potential, the aqueous Ce(III)/Ce(IV) redox couple could enable an increased redox flow battery voltage, and it is therefore part of several investigated redox systems, such as Zn-Ce, V-Ce, and H_2-Ce [7-10]. Due to the limited solubility, mixed acidic electrolytes have been developed with an increased cerium solubility to further improve the performance of Ce-based redox flow batteries [11]. In addition, cerium redox flow systems have also been proposed for hydrogen production [12].

Beyond its technological relevance, the electrochemical redox couple of dissolved Ce(III)/Ce(IV) ions, $\mathrm{Ce^{4+} + e^- \rightleftharpoons Ce^{3+}}$, has been subject of several fundamental studies [11, 13-20]. The investigation of its reaction kinetics is complicated by its high equilibrium potential, where essentially all electrode materials become oxidized. Gold is a preferred electrode material for this purpose because of its late onset of surface oxidation, which is just below the Ce(III)/Ce(IV) standard equilibrium potential. This enables to study the Ce(IV) reduction on a reduced gold electrode surface. However, the Ce(III) oxidation is generally observed in a potential range where the gold surface becomes oxidized. The different respective states of the gold electrode surface make it difficult to correlate the kinetic parameters determined for Ce(IV) reduction with the ones obtained for Ce(III) oxidation and to draw reliable conclusions about the involved reaction mechanism.

We circumvented these problems by investigating the kinetics of Ce(IV) reduction and Ce(III) oxidation within an identical potential range negative of the corresponding standard equilibrium potential, below the onset of gold surface oxidation. For this purpose, we performed separate experiments where only one of the species was present in the electrolyte at a time. We successfully determined very precise kinetic parameters of both Ce(IV) reduction and Ce(III) oxidation on a reduced gold electrode surface, which enabled a careful comparison with theoretical models. Our results reveal an exponential behavior of the kinetic currents for both reaction directions in perfect agreement with the Butler-Volmer model, but with a surprisingly large asymmetry. We show that the kinetic data cannot be satisfactorily described by Marcus theory models for electron transfer. Instead, we propose a mechanism that involves the field-induced dissociation of cerium–sulfate complexes as rate-determining step.

Although it occurs in the outer part of the electrochemical double-layer, it is strongly influenced by electrode material and surface properties, mediated by the electrostatic fields across the electrochemical double-layer.

Experimental

Experimental setup

A three-electrode glass cell setup was used. All experiments were performed in de-aerated, N_2-saturated electrolyte solutions at room temperature (≈ 25°C). A gold mesh was used as counter electrode and the reference electrode was a Hg/Hg_2SO_4 electrode (ALS Co. Ltd, Prod.-No. RE-2CP) with a saturated K_2SO_4 filling solution. The reference electrode was calibrated vs. the reversible hydrogen electrode (RHE) in 1 M H_2SO_4 (prepared from H_2SO_4, 96 %, Merck, Prod.-No. 1.00714). The working electrode was a polycrystalline gold disk (Au_{poly}) with a diameter of 5 mm and a geometric area of 0.196 cm^2 supplied by Pine Research Instrumentation.

Gold electrode pre-treatment

Before every experiment the gold disk was polished with 0.05 µm Al_2O_3 powder on a MicroCloth pad (Buehler) for several minutes and subsequently annealed at high temperature while dark red glowing in a 5% H_2/95% Ar mixture for 2 minutes using an induction heating setup. Then the electrode was immersed in 1 M H_2SO_4 and pre-treated by cyclic voltammetry (CV) between 0.70 and 1.45 V_{RHE} for 20 cycles at 20 mV/s. A CV was recorded from 0.70 to 1.44 V_{RHE} at 10 mV/s to acquire a representative CV of the gold electrode for background subtraction in the kinetic analysis. The roughness factor was determined to be 0.93 using the Cu underpotential deposition (Cu_{UPD}) charge measured between 0.22 and 0.62 V_{RHE} while cycling the electrode in 1 mM $CuSO_4$ (99.999%, Sigma Aldrich, Prod.-No. 203165) between 0.21 and 0.84 V_{RHE}. A specific charge of 370 µC/cm^2 was assumed [21] (average of the specific charge of the three low index facets). The determined value of the roughness factor is very close, but less than one, which is physically unreasonable. Taking into account realistic error margins of the Cu_{UPD} method, we consider the physical roughness factor to be essentially one, indicating that the annealing produced an almost perfectly flat Au_{poly} surface.

Kinetic RDE experiments

The kinetics of the Ce(III) oxidation and of the Ce(IV) reduction were investigated separately by rotating disk electrode (RDE) measurements in 1 mM and 10 mM solutions of either Ce(III) or Ce(IV) in 1 M H_2SO_4 ($Ce_2(CO_3)_3 \cdot 5H_2O$, 99.9 % trace metal, Sigma Aldrich, Prod.-No. 325503, and $Ce(SO_4)_2 \cdot H_2SO_4 \cdot H_2O$, 99.9 %, Sigma Aldrich, Prod.-No. 423351). Polarization curves were recorded between 0.70 and 1.44 V_{RHE} at 10 mV/s and RDE rotation rates of 400, 900, 1600, and 2500 rpm. To confirm that no significant changes occurred during the measurements, the polarization curves at 1600, 900 and 400 rpm were repeated and compared to the previous ones. All experiments were repeated 3 times for assessment of error margins and reproducibility. The Ohmic resistance for *IR*-correction was obtained from the high-frequency impedance determined by electrochemical impedance spectroscopy (EIS). To investigate the

influence of the Au surface oxide layer on the Ce(III)/ Ce(IV) kinetics, in one experimental series the upper potential limit was varied between 1.38 and 1.45 V_{RHE} for RDE measurements at 20 mV/s and 2500 rpm.

Data correction

The measured RDE currents were first corrected for the *IR*-drop with the Ohmic resistance *R* determined by EIS. Then the corresponding baseline CV currents were subtracted as determined in Ce-free 1 M H_2SO_4 electrolyte. Finally, the mass-transport influence was corrected. For the general case where both reaction directions influence the measured currents, i.e. especially near the equilibrium potential, the commonly applied simplified Koutecký-Levich equation with a potential-independent limiting current is not valid. Instead, the following general form must be used [22]:

$$\frac{1}{I} = \frac{1}{I_{kin}} + \frac{1}{I_{kin}}\omega^{-1/2}\left(k_a \frac{4.975*v^{1/6}}{D_R^{2/3}} + k_c \frac{4.975*v^{1/6}}{D_O^{2/3}}\right) \quad (1)$$

$$\frac{1}{I} = \frac{1}{I_{kin}} + \frac{1}{I_{kin}}\frac{func(E)}{\sqrt{\omega}} \quad (2)$$

where ω is the rotation rate (in rad/s), k_a and k_c the potential dependent reaction rates of the oxidation and reduction respectively, v the kinematic viscosity of the electrolyte and D_R and D_O the diffusion coefficients of the reduced and oxidized species. The dependence on the rotation rate, which is emphasized in Eq. (2) is used to determine the kinetic current: After *IR*- and CV correction, a Koutecký-Levich plot of $1/I$ vs. $1/\sqrt{\omega}$ is linearly fitted at each potential, as exemplarily shown in Fig. 1 for representative data sets from our experiments. An excellent linear fit of the data points was obtained. The extrapolated intercept of the fit with the y-axis yields the kinetic current in form of $1/I_{kin}$. Repeating this procedure for each potential yields the kinetic current I_{kin} as a function of the potential *E*, from which the Tafel plot of $\log_{10}(|I_{kin}|/\text{mA})$ vs. *E* is obtained. For Ce(III) oxidation analysis, the 400 rpm data was omitted, because it reduced the fit quality owing to the extremely small, and thus less precise, measured currents.

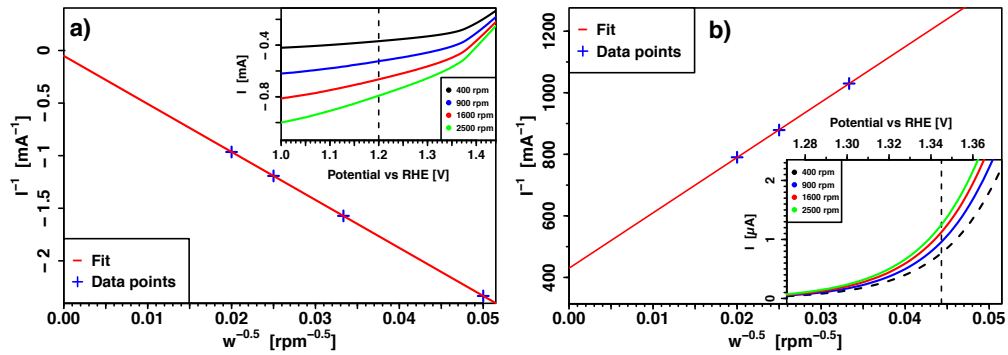

Fig. 1: Representative Koutecký-Levich plots of our experimental data taken at a) 1.20 V_{RHE} for the reduction of a 10 mM Ce(IV) solution and b) at 1.35 V_{RHE} for the oxidation of a 1mM Ce(III) solution.

It becomes clear from the inset of Fig. 1b that the general form (1)-(2) of the Koutecký-Levich equation was indeed required for the mass-transport correction in the present study: The apparent rotation dependence of the Ce(III) oxidation currents is not due to the mass transport of the Ce(III) reactant species to the electrode surface, but it is due to the influence of the back reaction of Ce(IV) species generated at the electrode surface. It is thus the mass transport of the Ce(IV) product species away from the electrode surface that produces the observed rotation dependence.

Kinetic data analysis

The kinetics of the electrochemical Ce(III)/Ce(IV) redox couple were analyzed using the Butler-Volmer equation. It is common to write the Butler-Volmer equation with the overpotential η:

$$I_{kin} = i_0 A(e^{\alpha_{anodic}\,\eta F/RT} - e^{-\alpha_{cathodic}\,\eta F/RT}) \qquad (3)$$

where $i_0 = nFk_0(C_R^B)^{\alpha_{cathodic}}(C_O^B)^{\alpha_{anodic}}$ is the exchange current density. Here, $n = 1$ is the number of transferred electrons, F is the Faraday constant, R the gas constant, T the temperature, A the electrode area, k_0 the reaction rate constant, and α_{anodic} and $\alpha_{cathodic}$ are the anodic and cathodic transfer coefficients, respectively. For one-step single-electron-transfer reactions, the transfer coefficients must add up to one, $\alpha_{cathodic} + \alpha_{anodic} = 1$, so they can be characterized by a single symmetry factor β:

$$\alpha_{anodic} = 1 - \beta \qquad (4)$$
$$\alpha_{cathodic} = \beta \qquad (5)$$

However, to avoid *a priori* assumptions regarding the reaction mechanism of the Ce(III)/Ce(IV) redox couple, we experimentally determined both parameters independently, and we refer to them as transfer coefficients in the following [23, 24].

The form (3) of the Butler-Volmer equation with the overpotential η has the disadvantage that the equilibrium potential must be defined for the actual reactant concentrations, i.e. both species must be simultaneously present in the experiment. This disadvantage can be circumvented using the Butler-Volmer equation in the general form:

$$I_{kin} = nFAk_0\left(C_R^B e^{\alpha_{anodic}\,(E-E^0)F/RT} - C_O^B e^{-\alpha_{cathodic}\,(E-E^0)F/RT}\right) \qquad (6)$$

As described in the previous section, mass-transport limitations to the electrode surface are corrected using the RDE method with Koutecký-Levich analysis to obtain the kinetic currents. Therefore, C_R^B and C_O^B refer to the bulk concentrations of Ce(III) and Ce(IV), respectively. Furthermore, we implicitly neglect transient time-dependent effects and assume a steady state at every electrode potential. This assumption is well justified for the slow scan rate of 10 mV/s employed during RDE measurements, as confirmed by the perfectly linear Koutecký-Levich plots, cf. Fig. 1.

Equation (6) is written with the fixed standard equilibrium potential E^0. Therefore, the reactant concentrations appear explicitly and equation (6) is valid with the electrode potential E on a fixed potential scale that does not depend on the concentrations of the oxidized and reduced species. In particular, this form of the Butler-Volmer equation remains valid if one of the bulk reactant concentrations is equal to zero. It thus allows measuring and analyzing the kinetics of Ce(III) oxidation and of Ce(IV) reduction separately by setting the concentration of either Ce(III) or Ce(IV) equal to zero in the bulk solution. As a great advantage, this enables studying both reaction directions in an identical potential range, i.e. for identical conditions of the catalyst/electrode surface. This approach allowed us to obtain precise and highly consistent kinetic parameters for both reaction directions on fully reduced Au electrodes even though the corresponding potential range lies entirely on the cathodic side of the standard equilibrium potential.

Setting once C_O^B and once C_R^B equal to zero in Eq. (6), we obtain the Tafel equations:

$$\log_{10}\left(I_{kin,O}\right) = \log_{10}(nFAk_0C_R^B) + \alpha_{anodic}(E - E^0)F/\left(RT\ln(10)\right) \quad (7)$$

$$\log_{10}\left(-I_{kin,R}\right) = \log_{10}(nFAk_0C_O^B) - \alpha_{cathodic}(E - E^0)\,F/\left(RT\ln(10)\right) \quad (8)$$

From the Tafel plot of $\log_{10}(I_{kin,O})$ of the Ce(III) oxidation, the anodic transfer coefficient α_{anodic} was determined from the slope of a linear fit according to eq. (7). The rate constant k_0 was determined from the extrapolation of the fitted curve to the measured standard equilibrium potential E^0. The same fitting procedure was performed for $\log_{10}(-I_{kin,R})$ of the Ce(IV) reduction to obtain the cathodic transfer coefficient $\alpha_{cathodic}$ and the rate constant k_0 according to eq. (8).

Density functional theory (DFT) computations

The potential of zero charge (PZC) of a gold (111) electrode in sulfuric acid with different surface adsorbate structures was obtained from density functional theory (DFT) computations with the Vienna *ab initio* simulation package (VASP) [25] using PAW pseudopotentials [26] and the GGA exchange-correlation functional in PBE form [27]. A plane-wave energy cutoff of 450 eV was chosen. In addition, the D3(BJ) [28, 29] van der Waals correction was used. Au slabs with the (111) surface orientation and 7 atomic layers were constructed, with the help of the pymatgen python package [30], from the Au bulk fcc cell with a relaxed lattice constant of 4.101 Å. For (hydr)oxide adsorbate calculations, supercells comprised the hexagonal (2×2) surface cell, containing 4 surface Au atoms per surface cell. For sulfate adsorbate calculations, supercells with the $(\sqrt{3} \times \sqrt{7})$ sulfate adsorbate structure [31-37] were used, containing 10 surface Au atoms per surface cell, and different numbers of co-adsorbed H_2O molecules were explicitly included. Adsorbates were placed symmetrically on both slab surfaces to cancel the overall supercell dipole. Reciprocal *k*-space was sampled with a Γ-centered 3x5x1-mesh for sulfate-adsorbate supercells and a 5x5x1-mesh for (hydr)oxide adsorbate supercells. Coordinates were relaxed, keeping the innermost Au-layer fixed, until forces were smaller than 0.01 eV/Å.

Relaxed coordinates of the different systems are given in the Supporting Information. Supercells comprised 20–25 Å of vacuum/electrolyte region between periodic slab images. The aqueous electrolyte environment was taken into account using the VASPsol implicit solvent model [38] with default $\varepsilon_r = 78.4$ for water. To compute the equilibrium potential of Au(111) surface oxidation, the contribution of the charged electrochemical interface was included using the homogeneous background method [39]. In short, the electron number N of the supercell was varied with respect to the electron number of the neutral cell N_0, including a homogeneous counter-charge background. From the DFT energy E_{DFT}, the corresponding electrochemical free energy $E_{\mathrm{free}} = E_{\mathrm{DFT}} - (N - N_0)E_{\mathrm{Fermi}}$ was computed with the chemical potential equal to the Fermi energy E_{Fermi}. Oxidation potentials were determined from the electrochemical free energies using the computational hydrogen electrode (CHE) [40], i.e. molecular H_2, as reference, including vibrational free energies at $T = 25°\mathrm{C}$ obtained from DFT vibrational analysis. The free energies of hydrogen gas and liquid water at $T = 25°\mathrm{C}$ were computed from DFT ground-state energies of single molecules including vibrational zero-point energy (ZPE), adding the corresponding tabulated entropic $-TS$ contributions[41], the tabulated gas phase enthalpy differences $H°(298.15\ \mathrm{K}) - H°(0)$ [42], and the tabulated heat of condensation $H^{\circ}_{\mathrm{H2O(liq)}}(298.15\ \mathrm{K}) - H^{\circ}_{\mathrm{H2O(gas)}}(298.15\ \mathrm{K})$[41].

Results and Discussion

Cyclic voltammetry

Fig. 2 shows the CV of Au_{poly} in 1 M H_2SO_4. Oxidation of the gold surface starts in the positive-going scan around 1.35 V_{RHE} with a sharp increase at 1.38 V_{RHE}. Reduction of the oxidized surface occurs in the negative-going scan below 1.35 V_{RHE} and is largely completed around 1.05 V_{RHE}. The upper potential was limited to 1.44 V_{RHE} in order to maintain a stable CV and minimize surface reorganization due to repeated oxidation and reduction cycles.

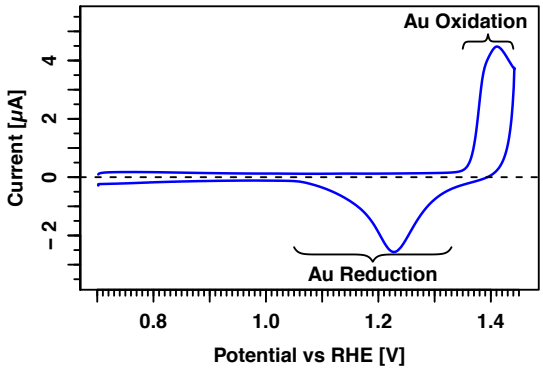

Fig. 2: CV of Au_{poly} in 1 M H_2SO_4 from 0.70 to 1.44 V_{RHE} at 10 mV/s.

Standard equilibrium potential

The standard equilibrium potential of the Ce(III)/Ce(IV) redox couple was determined both via the open circuit potential and via the zero-current intercept of RDE curves in a 10 mM equimolar Ce(III)/Ce(IV) solution. A value of E^0 = 1.444 V_{RHE} was obtained for both methods in

agreement with reported literature values [1, 8, 43, 44]. Note that 1 M H_2SO_4, as used in our study, corresponds to pH≈0, and thus RHE≈SHE.

Kinetics on reduced Au surface

The kinetics of both the Ce(III) oxidation and the Ce(IV) reduction were determined on the reduced gold surface in the same potential range below 1.35 V_{RHE} from the positive-going scans of RDE measurements. Table 1 compiles the resulting kinetic parameters. For Ce(III) oxidation, only results from 1 mM Ce(III) solutions are presented, because we observed that higher Ce(III) concentrations lead to passivation of the Au electrode, possibly due to impurities in the reagent.

Fig. 3c shows the Tafel plot for the Ce(IV) reduction in 10 mM Ce(IV) solution. The plot revealed an excellent linearity over a wide potential range between 1.00 – 1.35 V_{RHE} proving that the kinetic current of the Ce(IV) reduction perfectly followed the exponential form of the Butler-Volmer equation on the reduced Au surface. The fits of three independent data sets in the range 1.07 – 1.35 V_{RHE} yielded a very small value of the cathodic transfer coefficient $\alpha_{cathodic} = 0.154 \pm 0.001$ corresponding to a large Tafel slope of $\ln(10)\,RT/(F\alpha_{cathodic}) = 384 \pm 3$ mV/dec (inverse of the slope in Fig. 3c). An excellent agreement was found between the kinetic parameters determined from 1 mM and from 10 mM Ce(IV) solutions, cf. Table 1. This supports the underlying assumption of first-order Ce(IV) reduction kinetics in the Butler-Volmer equation (6).

Table 1: Determined kinetic parameters in 1 M H_2SO_4.

Solution (reaction)	$k_0/10^{-3}$ [cm/s]	$\alpha_{cathodic}$	α_{anodic}
10 mM Ce(IV) (reduction)	3.8 ± 0.4	0.154 ± 0.001	—
1 mM Ce(IV) (reduction)	3.9 ± 0.5	0.161 ± 0.006	—
1 mM Ce(III) (oxidation)	3.8 ± 1.6	—	0.84 ± 0.02

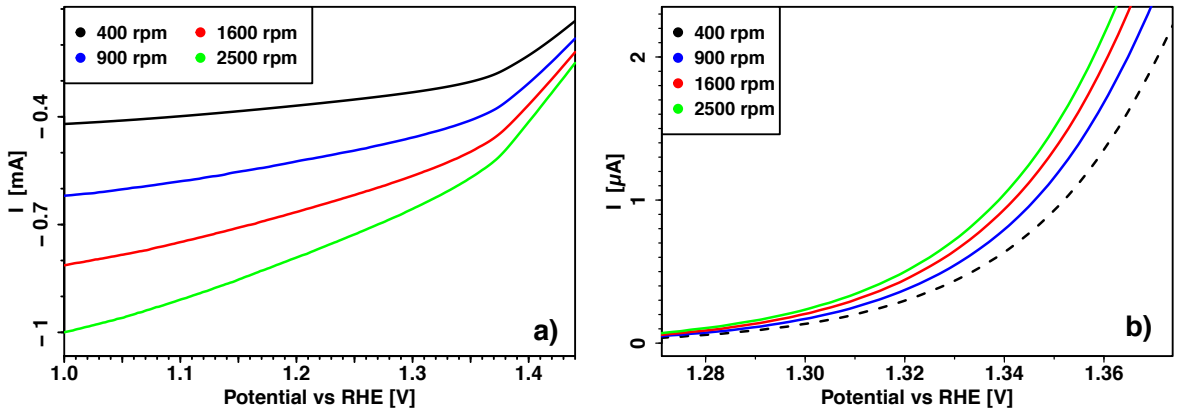

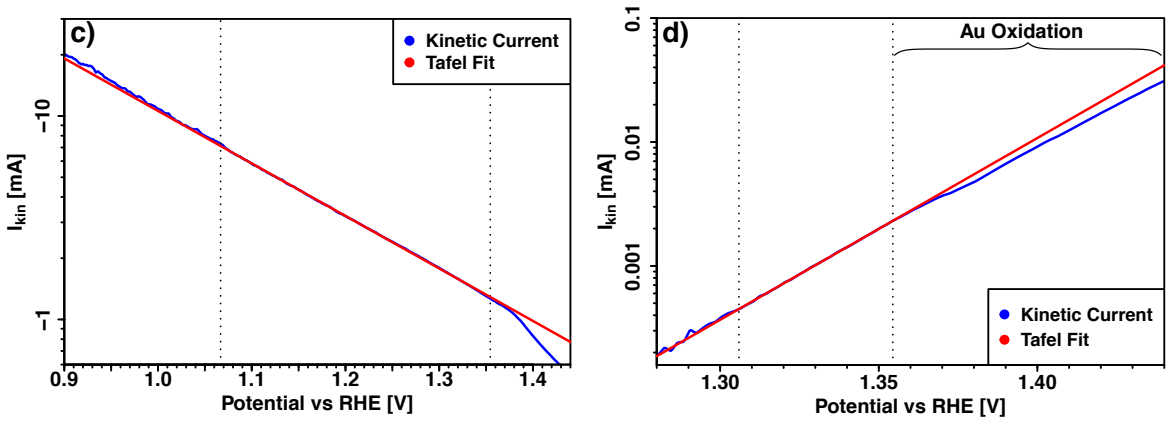

Fig. 3: Tafel plots of (c) the Ce(IV) reduction (10 mM) and (d) the Ce(III) oxidation (1 mM). Corresponding RDE-currents (*IR*- and CV-corrected) at different RDE rotation rates are shown in (a) and (b), respectively.

The Tafel plot for the Ce(III) oxidation in 1 mM Ce(III) solution, c.f. Fig. 3d, also showed excellent linearity in the potential range below 1.35 V_{RHE} proving that the kinetic current of the Ce(III) oxidation perfectly followed the exponential form of the Butler-Volmer equation on the reduced Au surface. The fits of three independent data sets in the range 1.31 – 1.35 V_{RHE} yielded an anodic transfer coefficient $\alpha_{anodic} = 0.84 \pm 0.02$ corresponding to a Tafel slope of $\ln(10)\, RT/(F\alpha_{anodic}) = 70 \pm 2$ mV/dec (inverse of the slope in Fig. 3d).

Table 2 presents a comparison of our results with other published data [13-16] for the Ce redox couple on gold electrodes. The large scattering of previously reported anodic transfer coefficients α_{anodic} could result from the fact that previous studies measured Ce(III) oxidation at potentials where the Au surface is already partially oxidized. Thus, to the best of our knowledge, our study is the first to determine precise kinetic parameters of Ce(III) oxidation on a completely reduced Au surface. Our value of the cathodic transfer coefficient $\alpha_{cathodic}$ is lower than previously reported values, and our values of the kinetic rate constant are larger by a factor 2 – 100 than previously reported kinetic rate constants. As discussed and substantiated in the following, our results represent highly precise and reliable kinetic parameters of the Ce redox couple on Au_{poly}.

Table 2: Comparison with literature results for the Ce redox couple on gold electrodes in sulfuric acid. (n.r. = not reported)

Ref.	Electrolyte	Transfer coef.	$k_0/10^{-3}$ [cm/s]
This work	1 M H_2SO_4 + 0.001 / 0.01 M Ce(IV) 1 M H_2SO_4 + 0.001 M Ce(III)	$\alpha_{cathodic} = 0.157$ $\alpha_{anodic} = 0.84$	3.9 3.8
[14]	1 M H_2SO_4 + 0.01 M Ce(III) + 0.01 M Ce(IV)	$\alpha_{cathodic}$ n.r. $\alpha_{anodic} = 0.65$	0.4
[15]	1 M H_2SO_4 + 0.001 M Ce(III) + 0.01 M Ce(IV)	$\alpha_{cathodic} = 0.33$ α_{anodic} n.r.	0.2

[16]	0.5 M H_2SO_4 + 0.018 M Ce(III) + 0.018 M Ce(IV)	$\alpha_{cathodic} = 0.19$ $\alpha_{anodic} = 0.12$	2.1 1.4
[13]	1 M H_2SO_4 + 0.01 M Ce(III)	$\alpha_{cathodic}$ n.r. $\alpha_{anodic} = 0.16$	 0.05

Our measured values of the kinetic parameters establish a perfect quantitative agreement with the Butler-Volmer equation (6): Firstly, the exponential form of the current–voltage relationship is accurately followed by the kinetic currents of both Ce(III) oxidation and Ce(IV) reduction in the potential range of a reduced Au surface. Secondly, the values of the reaction rate constant k_0 determined separately from Ce(III) oxidation and from Ce(IV) reduction experiments agree remarkably, given the fact that the fitted kinetic current of the Ce(III) oxidation was extrapolated over more than one order of magnitude in order to obtain k_0. Thirdly and most remarkably, in spite of their very different values, the anodic and cathodic transfer coefficients perfectly add up to one, $\alpha_{cathodic} + \alpha_{anodic} = 1.00 \pm 0.02$, as required for the simultaneous fulfillment of both the Butler-Volmer equation and the Nernst equation. Finally, all kinetic parameters were extracted by using experimental data of the forward and backward reaction from the same potential region, thereby excluding potential-dependent differences of the Au surface state. Additionally, very small statistical error margins prove the reproducibility of the experiments and the reliability of the obtained values.

A first interpretation of our results could be that the electrochemical Ce(III)/Ce(IV) redox couple in sulfuric acid on a reduced polycrystalline gold surface is a one-step single-electron-transfer reaction with a symmetry factor $\beta = 0.157$, i.e. $\alpha_{cathodic} = \beta$ and $\alpha_{anodic} = (1 - \beta)$. However, such an extreme asymmetry is surprising in light of typically encountered values of symmetry factors closer to 0.5 [45-48], corresponding to approximately symmetric oxidation and reduction branches. Nevertheless, it was emphasized that significant asymmetries can arise under certain conditions [49, 50]. Early theories of electron-transfer reactions predict a symmetry factor equal to 0.5 around the standard equilibrium potential and for sufficiently large solvation energies [51-55]. If electron transfer is associated with significant intramolecular reorganization, strong deviations of β from 0.5 are possible, with values down to 0.2 and up to 0.8 having been reported for certain redox couples [50]. Our observed asymmetry for the Ce(III)/Ce(IV) redox couple in sulfuric acid with cathodic and anodic transfer coefficients < 0.2 and > 0.8, respectively, challenges even the most extreme asymmetries previously reported for single-electron-transfer reactions.

Moreover, the Butler-Volmer equation has a semi-empirical nature based on the assumption that the intersecting energy hypersurfaces of the reaction are linear. Microscopic electron-transfer theories, however, predict Tafel plots with a certain curvature. The perfect and highly asymmetric Butler-Volmer kinetics revealed by our results represent a challenge for electron-transfer models to be analyzed in the following. We will first demonstrate that the assumption of a rate-determining single-electron-transfer step fails to satisfactorily describe our data. We

will then show that a field-dependent dissociation of cerium–sulfate complexes in the outer part of the electrochemical double-layer is likely rate-limiting.

Electrochemical outer-sphere electron transfer

Marcus theory [51, 54] is microscopically founded on the prominent role of the solvation and complexation shells of reactants and products for the electron-transfer step, and it predicts an approximately parabolic shape of the energy hypersurfaces of reactant and product that results both from the electrostatic energy of the ion embedded in the dielectric solvent [52] and from the harmonic energy approximation for the internal configurational degrees of freedom of the complex ion [54]. Marcus theory applies to "outer-sphere" electron transfer where the solvation and complexation shell of the reacting species remains intact during the electron-transfer step. Typically, electrochemical electron-transfer reactions between an electrode and dissolved ionic redox species, such as the present Ce redox couple, are assumed to fall into this category.

Within the framework of the Marcus theory, the timescale of the electron-transfer step is considered to be extremely short compared to the timescale of changes in the ligand coordination shell of the reacting Ce(III)/(IV) complex. Therefore, the coordination number remains constant during the electron-transfer reaction. Because several different cerium complexes coexist in 1 M H_2SO_4 solution [56-58], the reaction can proceed via three different routes:

$$[\mathrm{Ce}]_{\mathrm{aq}}^{4+} + \mathrm{e}^- \rightleftharpoons [\mathrm{Ce}]_{\mathrm{aq}}^{3+} \qquad \text{(Reaction 1)}$$

$$[\mathrm{Ce(SO_4)}]_{\mathrm{aq}}^{2+} + \mathrm{e}^- \rightleftharpoons [\mathrm{Ce(SO_4)}]_{\mathrm{aq}}^{+} \qquad \text{(Reaction 2)}$$

$$[\mathrm{Ce(SO_4)_2}]_{\mathrm{aq}} + \mathrm{e}^- \rightleftharpoons [\mathrm{Ce(SO_4)_2}]_{\mathrm{aq}}^{-} \qquad \text{(Reaction 3)}$$

Based on published experimental equilibrium constants [56-58], we computed the relative concentrations and the energetic alignment of the relevant Ce complex ions in 1 M H_2SO_4, as described in detail in the Supporting Information and shown in Supporting Information Fig. S1. Because Ce(III) does not form a detectable tri-sulfate complex, there exists no direct redox couple for the most stable Ce(IV) tri-sulfate complex. The Ce(IV) mono-sulfate complex and the Ce(IV) uncomplexed species lie energetically very high. Therefore, we focus on the pathway involving the di-sulfate complexes, Reaction (3), in the following. This choice will later be critically reviewed in the discussion of the electrochemical dissociation field effect. It must be noted that the specific complex couple $[\mathrm{Ce(SO_4)_2}]_{\mathrm{aq}}$ / $[\mathrm{Ce(SO_4)_2}]_{\mathrm{aq}}^{-}$ is characterized by a standard equilibrium potential E_0^0 corresponding to equimolar concentrations of $[\mathrm{Ce(SO_4)_2}]_{\mathrm{aq}}$ and $[\mathrm{Ce(SO_4)_2}]_{\mathrm{aq}}^{-}$. A value of $E_0^0 = 1.517\ \mathrm{V_{RHE}}$ results from inserting our experimentally measured value of the overall standard equilibrium potential $E^0 = 1.444\ \mathrm{V_{RHE}}$ and the relative concentrations $rc_{[\mathrm{Ce(SO_4)_2}]_{\mathrm{aq}}} = 0.048$ and $rc_{[\mathrm{Ce(SO_4)_2}]_{\mathrm{aq}}^{-}} = 0.827$, cf. Supporting Information Fig. S1, into the Nernst equation $E^0 = E_0^0 + (RT/F)\ \ln(rc_{[\mathrm{Ce(SO_4)_2}]_{\mathrm{aq}}}/rc_{[\mathrm{Ce(SO_4)_2}]_{\mathrm{aq}}^{-}})$.

For each internal configurational degree of freedom of the reacting solvated complex ion, the basic symmetric Marcus-Hush (SMH) model [51, 54, 59-61] assumes identical force constants (i.e. identical parabola curvatures) for the oxidized and the reduced complex ion. However, our results reveal highly asymmetric kinetics of the Ce redox couple. The symmetry assumption is relaxed in the asymmetric Marcus-Hush (AMH) model [62-64] that uses a first order correction for the case that certain degrees of freedom have different force constants/curvatures in the oxidized and the reduced complex ion, respectively. In addition to SMH and AMH, we also tested a "generalized" asymmetric Marcus-Hush (GAMH) model that considers the intercept of two arbitrarily asymmetric parabolas. The detailed equations for activation energies and kinetic currents corresponding to these Marcus-theory flavors, as well as the derivation of the GAMH model, are presented in the Supporting Information. We fitted the SMH, AMH, and GAMH models to our experimentally determined kinetic currents of the Ce(IV) reduction, both using the simple form of $I_{kin,\mathrm{R}}$ without integral (w/o integral), as well as the integral form, Supporting Information Equations (S20) and (S21), respectively. Because of the divergence of the integral for the AMH model, the latter was excluded at this level. The value of $E_0^0 = 1.517\ \mathrm{V_{RHE}}$ was fixed at the standard equilibrium potential of the di-sulfate complex couple, Reaction (3). More details about the fitting procedure are given in the Supporting Information.

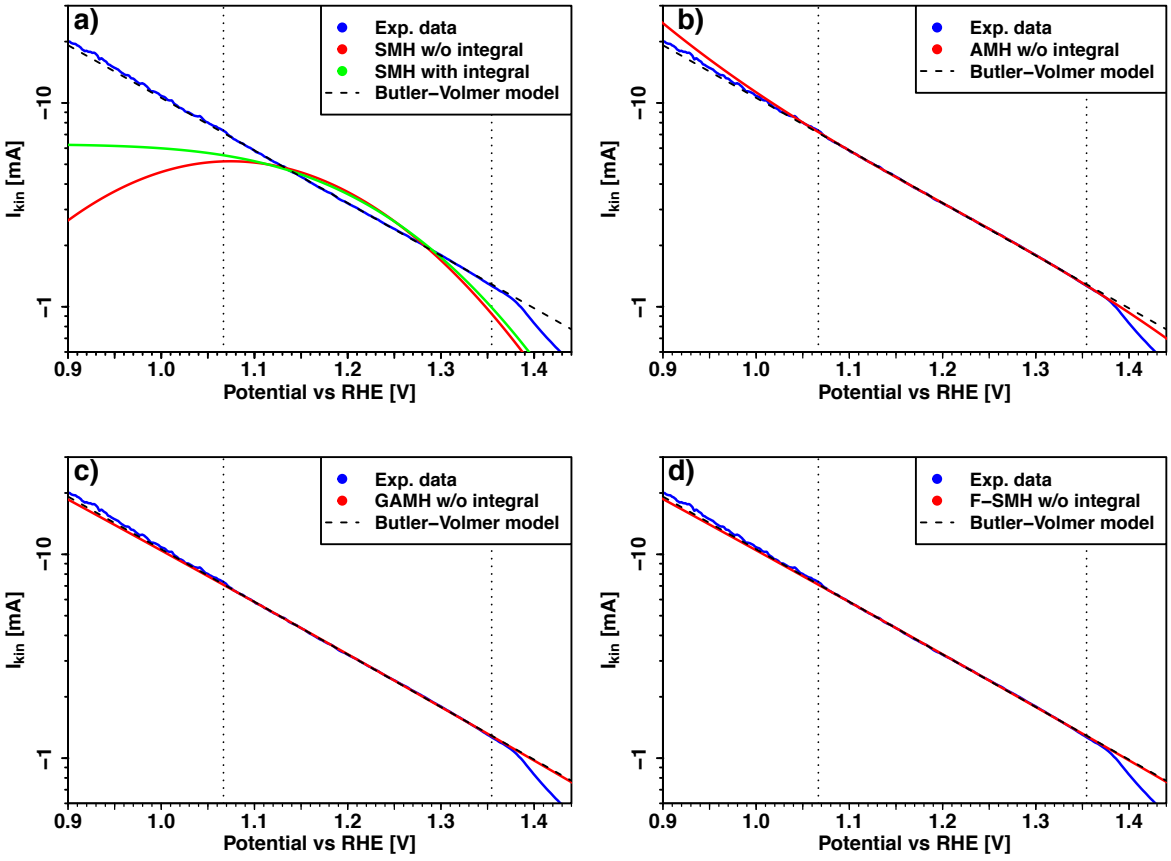

Fig. 4: Fits of SMH (a), AMH (b), GAMH (c), and Frumkin-SMH (d) models to our experimentally determined kinetic current of the Ce(IV) reduction on Au_{poly}. The dashed line shows the linear Tafel fit with the Butler-Volmer model.

Fig. 4 presents the resulting fits and Table 3 the fitted parameters, averaged over all independent Ce(IV) reduction runs. The SMH model, both w/o integral and with integral, yields a very poor fit to the experimental data, cf. Fig. 4a. This is not surprising, because the highly asymmetric nature of our experimental kinetic currents cannot be represented by the symmetric parabola model underlying SMH. In contrast, the AMH (w/o integral) model, Fig. 4b, provides a very good fit of the experimental data. However, this agreement must be regarded as the result of an unphysical behavior of the AMH model, because the fitted parameters, cf. Table 3, lie outside its range of validity: In the more negative part of the fitted potential range, the second term in Supporting Information Equation (S17) becomes equal or even larger than the first term. Because the AMH model is based on a perturbative approach, the model remains valid only as long as the second term is a first order correction to the leading term, and higher order terms can be neglected. For the fitted AMH parameters, this is clearly violated, and it results in an unphysical bending up of the fitted AMH curve in the more negative part of the potential range. Thus, the asymmetry of our experimental kinetic currents is too strong for the perturbative AMH model. Therefore, we developed the "generalized" asymmetric Marcus-Hush (GAMH) model, Supporting Information Equation (S18), that considers two arbitrarily asymmetric free energy parabolas for the reactant and product state, respectively. Although this model produced a very good fit, cf. Fig. 4c, the fitted reorganization energy of the reduced complex $[\mathrm{Ce}(\mathrm{SO}_4)_2]^-_{\mathrm{aq}}$ was $\lambda_{\mathrm{red}} \approx 120$ eV, cf. Table 3, both with and w/o the integral in the kinetic current equation. Clearly, such large value for the reorganization energy is not physically reasonable. Also, the fitted value for the asymmetry ratio ω_{R} appears too extreme to be physically meaningful. Based on molecular dynamics simulations, it has been reported[65] that reorganization energies can, in fact, strongly vary when the charge state of a dissolved species changes from 0 to -1, but the corresponding factors were at most two. We thus conclude that neither the simple form (w/o integral) nor the integral form of SMH, AMH, and GAMH can satisfactorily explain the highly asymmetric Butler-Volmer-behavior of our experimental data.

Table 3: Fitting results for the parameters of the different models, averaged over all independent Ce(IV) reduction runs. Presented are the results both for the simple version (w/o integral) and for the integral version, Supporting Information Equations (S20) and (S21), respectively.

Model	λ OR λ_{ox} | λ_{red}	γ (AMH)	ω_{R} (GAMH)	$E^{\mathrm{eff}}_{\mathrm{PZC}}$	κ (Frumkin)
SMH (w/o integral)	0.45 eV	—	—	—	—
SMH (integral)	0.30 eV	—	—	—	—
AMH (w/o integral)	0.92 eV	−1.09	—	—	—
AMH (integral)	—	—	—	—	—
GAMH (w/o integral)	4.6 eV | 121 eV	—	0.038	—	—
GAMH (integral)	4.6 eV | 123 eV	—	0.037	—	—
F-SMH (w/o integral)	0.64 eV	—	—	2.4 V_{RHE}	0.86
F-SMH (integral)	0.34 eV	—	—	fixed at 2.4 V_{RHE}	0.84

Frumkin-Marcus-Hush model

To further explore the origin of the intriguing behavior of the electrochemical Ce(III)/Ce(IV) redox kinetics, we include the Frumkin effect into our consideration. Up to now, we have implicitly assumed that the reacting complex is located fully on the electrolyte side of the electrochemical double-layer, i.e. the entire electrostatic potential drop occurs in between the electrode and the position of the reacting complex. Consequently, the reaction free energy of the electron-transfer step is affected by the entire electrode potential term $e(E - E_0^0)$ as expressed in Supporting Information Equation (S19). If, however, the reacting complex is located *within* the electrochemical double-layer, it will experience only a fraction of the electrostatic potential drop, and thus the electrode potential. In addition, the local electrostatic potential at the reaction location will modify the local equilibrium concentration of the reacting complex. These two effects are called Frumkin effect or Frumkin correction [66-70]. In the basic approach, the electron transfer is assumed to occur when the reacting complex, including its solvation and complexation shell, is located at its distance of closest approach from the electrode, which defines the plane of closest approach (PCA). Identifying the PCA with the outer Helmholtz plane (OHP) of the Gouy-Chapman-Stern model of the electrochemical double-layer, the electrostatic potential Φ_{PCA} at the PCA, measured w.r.t. to the electrostatic (inner) potential in the bulk electrolyte, is given by [69] $\Phi_{\mathrm{PCA}} = \kappa(E - E_{\mathrm{PZC}})$, with $\kappa = \mathcal{C}_{\mathrm{tot}}/\mathcal{C}_{\mathrm{out}}$ being the ratio of the total double-layer capacitance $\mathcal{C}_{\mathrm{tot}}$ over the diffuse (outer) layer capacitance $\mathcal{C}_{\mathrm{out}}$, and where E is the electrode potential and E_{PZC} is the potential of zero charge (PZC), i.e. the electrode potential where no charge is accumulated in the electrochemical double-layer. Note that the *diffuse* layer, i.e. the outer part of the electrochemical double-layer according to the Gouy-Chapman-Stern model, must be clearly distinguished from the *diffusion* layer. The latter corresponds to the uncharged layer across which species diffuse from the bulk of the electrolyte to the electrode surface. These diffusion effects are corrected for by the RDE method and do not affect the kinetic currents obtained after Koutecký-Levich correction.

The applicability of the Gouy-Chapman-Stern model must be questioned for the large sulfuric acid concentrations used in our experiments. Moreover, as discussed below, our experimental potential range is significantly negative of the PZC, and sulfate adsorbates strongly contribute to the electrostatic potential distribution at the gold electrode surface. However, also for our experimental conditions, a linearized relation can be well justified,

$$\Phi_{\mathrm{PCA}} = \Phi_{\mathrm{PCA}}^0 + \kappa(E - E_{\mathrm{PZC}}) \qquad (9)$$

with a proportionality factor κ quantifying the sensitivity of Φ_{PCA} towards changes of the electrode potential E, as a result of the free charges in the diffuse outer layer that scale with $(E - E_{\mathrm{PZC}})$. Strictly speaking, we will therefore use the symbol E_{PZC} and the abbreviation "PZC" to denote the potential of zero *free* charge throughout the following. The sulfate adsorbate layer is entirely static in the potential range of our kinetic measurements, which is

demonstrated by the extremely flat capacitive currents of the gold electrode CV in the respective potential range, shown in Fig. 2. The static sulfate adsorbate layer contributes a constant Φ_{PCA}^{0} to the electrostatic potential at the PCA. From a mathematical perspective, Equation (9) precisely derives from a Taylor-series expansion of the general relation $\Phi_{\mathrm{PCA}}(E)$ around a center E_{c} of the experimental potential range (in our case around $1.2\ \mathrm{V_{RHE}}$), where $\kappa = \frac{\mathrm{d}}{\mathrm{d}E}\Phi_{\mathrm{PCA}}(E_{\mathrm{c}})$ is the first derivative at E_{c} and $\Phi_{\mathrm{PCA}}^{0} = \Phi_{\mathrm{PCA}}(E_{\mathrm{c}}) - \kappa(E_{\mathrm{c}} - E_{\mathrm{PZC}})$. Higher-order terms of the expansion can be neglected as long as $\frac{\mathrm{d}}{\mathrm{d}E}\Phi_{\mathrm{PCA}}$ remains approximately constant within the experimental potential range, which we assume to be fulfilled. Note that Equation (9) can be recast in the form $\Phi_{\mathrm{PCA}} = \kappa(E - E_{\mathrm{PZC}}^{\mathrm{eff}})$ with an effective PZC parameter $E_{\mathrm{PZC}}^{\mathrm{eff}} = E_{\mathrm{PZC}} - \Phi_{\mathrm{PCA}}^{0}/\kappa$ that is shifted w.r.t. E_{PZC}.

We combine Marcus-theory and Frumkin effect in a Frumkin-SMH (F-SMH) model. The local potential Φ_{PCA} w.r.t. the bulk electrode potential changes the relative parabola alignment to $e(E - E_0^0 - \Phi_{\mathrm{PCA}})$. In combination with Equation (9), the SMH activation energy, Supporting Information Equation (S16), then turns into

$$\text{F-SMH} \qquad \Delta G_{\mathrm{R/O}}^{\ddagger}(\varepsilon) = \frac{\lambda}{4}\left(1 \pm \frac{\varepsilon + e\left(E - E_0^0 - \kappa(E - E_{\mathrm{PZC}}^{\mathrm{eff}})\right)}{\lambda}\right)^2 \qquad (10)$$

In addition, the local equilibrium concentration of the reactant complex changes to

$$C_{\mathrm{O/R}}^{\mathrm{PCA}} = C_{\mathrm{O/R}}^{\mathrm{B}} \exp\left[-\mathrm{z}_{\mathrm{O/R}} e \Phi_{\mathrm{PCA}}/kT\right] = C_{\mathrm{O/R}}^{\mathrm{B}} \exp\left[-\frac{\mathrm{z}_{\mathrm{O/R}} e}{kT}\kappa(E - E_{\mathrm{PZC}}^{\mathrm{eff}})\right] \quad (11)$$

where $\mathrm{z}_{\mathrm{O/R}}$ are the charges of the oxidized and reduced complex, respectively. The reacting complex concentration is part of the pre-exponential factor in Supporting Information Equations (S20) and (S21), which, including the Frumkin effect, therefore turn into

$$I_{kin,\mathrm{R/O}} = \mp B_{\mathrm{R/O}} \exp\left[-\frac{\mathrm{z}_{\mathrm{O/R}} e}{kT}\kappa(E - E_{\mathrm{PZC}}^{\mathrm{eff}})\right] \exp\left[-\Delta G_{\mathrm{R/O}}^{\ddagger}(\varepsilon = 0)/kT\right] \qquad (12)$$

and

$$I_{kin,\mathrm{R/O}} = \mp B_{\mathrm{R/O}} \exp\left[-\frac{\mathrm{z}_{\mathrm{O/R}} e}{kT}\kappa(E - E_{\mathrm{PZC}}^{\mathrm{eff}})\right] \int_{-\infty}^{+\infty} \frac{\exp\left[-\Delta G_{\mathrm{R/O}}^{\ddagger}(\varepsilon)/kT\right]}{1 + \exp[\mp\varepsilon/kT]}\,\mathrm{d}\varepsilon \qquad (13)$$

Note that the Frumkin effect enters twice into these equations, once in the first exponential due to the concentration factor, and once in the activation energy of the second exponential. Therefore, even for $\mathrm{z}_{\mathrm{O/R}} = 0$, the Frumkin effect acts as part of the F-SMH activation energy, Equation (10).

We fitted the Frumkin-Marcus-Hush model to our experimentally determined kinetic currents of the Ce(IV) reduction on $\mathrm{Au_{poly}}$, using $\mathrm{z_O} = 0$ for the reacting Ce(IV) di-sulfate

complex. Results are presented in Fig. 4d and Table 3. A very good agreement between fit and data was obtained for both versions, with and w/o integral, Equation (13) and (12), respectively. However, this required a very large fitted value of κ around 0.84 – 0.86. Since κ is the fraction of the electrostatic potential drop in the outer part of the double-layer, i.e. between PCA and bulk electrolyte, such large value means that the PCA lies very close to the electrode, which will be critically assessed below. The effective PZC parameter was fitted for the F-SMH version w/o integral and a value of $E_{\mathrm{PZC}}^{\mathrm{eff}} = 2.4\ \mathrm{V_{RHE}}$ was obtained. This value was fixed for the fitting of the F-SMH integral version. At first glance, such large value appears questionable and in contradiction to the PZC values < 0.6 V_{SHE} for common Au surface orientations [71-73] (note RHE≈SHE in the present study). However, specific adsorption of sulfate at the Au surface is known to occur in sulfuric acid [34, 74], precisely in the potential range where we determined the Ce(III)/Ce(IV) redox kinetics, which can significantly alter the PZC and also produce a non-zero Φ_{PCA}^{0} that shifts $E_{\mathrm{PZC}}^{\mathrm{eff}}$ w.r.t. the PZC, as discussed above.

Table 4: Aqueous work function W_{aq} and PZC E_{PZC} from DFT computations for different Au (111) surface adsorbate structures in implicit water environment.

Surface structure	W_{aq}	E_{PZC}
Au (111)	4.95 eV	$0.51\ \mathrm{V_{SHE}}$
Au (111) + 0.2 $(SO_4)_{ads}$	6.97 eV	$2.53\ \mathrm{V_{SHE}}$
Au (111) + 0.2 $(SO_4)_{ads}$ + 1 $(H_2O)_{co\text{-}ads}$	6.44 eV	$2.00\ \mathrm{V_{SHE}}$
Au (111) + 0.2 $(SO_4)_{ads}$ + 2 $(H_2O)_{co\text{-}ads}$	6.17 eV	$1.73\ \mathrm{V_{SHE}}$
Au (111) + (1/4) O_{ads}	5.36 eV	$0.92\ \mathrm{V_{SHE}}$
Au (111) + (1/2) O_{ads}	5.89 eV	$1.45\ \mathrm{V_{SHE}}$

We performed DFT calculations to test the plausibility of the fitted $E_{\mathrm{PZC}}^{\mathrm{eff}}$ for the sulfate-covered Au electrode. For this purpose, we chose the most stable Au (111) surface orientation as a model and constructed the ordered $(\sqrt{3} \times \sqrt{7})$ sulfate adsorbate structure with 0.2 adsorbed $(SO_4)_{ads}$ per surface Au atom that was reported from experimental STM studies [31-35] for the potential range above ≈1.05 V_{SHE}. Recently published experimental and computational results[35, 36] clearly proved sulfate as adsorbed species, rather than bisulfate, and the stable co-adsorption of two water molecules per adsorbed sulfate anion. Accordingly, we performed three different calculations including 0, 1, and 2 co-adsorbed explicit H_2O molecules per $(SO_4)_{ads}$ in addition to the implicit water environment. Our relaxed structures are given in the Supporting Information. Using an absolute SHE reference work function of $4.44\ \mathrm{eV}$ [75], we calculated the potential of zero charge $E_{\mathrm{PZC}} = (W_{\mathrm{aq}}/\mathrm{eV} - 4.44)\ \mathrm{V_{SHE}}$ from the work function W_{aq} in aqueous environment obtained from DFT computations. The results are presented in Table 4. Our reference values for the aqueous work function and PZC of the bare Au(111) surface are in good agreement with literature values [71, 76]. For the Au (111)–$(SO_4)_{ads}$ surfaces, we find PZC values ranging from 1.73 – 2.53 V_{SHE}, depending on the number of explicit H_2O molecules included in the simulation. Although our experiments were performed on a polycrystalline Au electrode and not on Au (111), this computed range of PZC values provides support for the value of $E_{\mathrm{PZC}}^{\mathrm{eff}} = 2.4\ \mathrm{V_{RHE}}$

(note RHE≈SHE in the present study) obtained from the F-SMH fit to our experimental data for the Ce(III)/Ce(IV) redox couple on Au electrodes in sulfuric acid. The negative charges of the sulfate adsorbates would yield $\Phi_{\mathrm{PCA}}^{0} \leq 0$, and thus $E_{\mathrm{PZC}}^{\mathrm{eff}} \geq E_{\mathrm{PZC}}$, in agreement with the computational results when co-adsorbed H_2O are included.

At the same time, however, the question for the plausibility and reason behind the exceptionally large fitted value of κ around 0.84 – 0.86 is emphasized. The potential range of our experimental analysis is significantly negative of the PZC. Typically, for molar electrolyte concentrations and a strongly charged electrochemical double-layer, the majority of the electrostatic potential drop occurs *within* the OHP [77-79], and we would rather expect a very low value of κ, possibly around 0.1. The fact that our fitted value of κ is almost equal to the value of $1 - \alpha_{cathodic}$ means that in the F-SMH model, the Frumkin part must shoulder the entire asymmetry of the transfer coefficients. As discussed above, within the Gouy-Chapman-Stern model, $\kappa = \mathcal{C}_{\mathrm{tot}}/\mathcal{C}_{\mathrm{out}}$ is the ratio of the total double-layer capacitance $\mathcal{C}_{\mathrm{tot}}$ over the diffuse (outer) layer capacitance $\mathcal{C}_{\mathrm{out}}$. Changing the latter would thus change κ, and, within the F-SMH model, directly affect the observed asymmetry. According to the Gouy-Chapman model, $\mathcal{C}_{\mathrm{out}} \propto 1/\lambda_{\mathrm{D}}$ is inversely proportional to the Debye length[80], so $\kappa \propto \lambda_{\mathrm{D}}$ approximately. The Debye length, in turn, is proportional to the square root of our sulfuric acid concentration, $\lambda_{\mathrm{D}} \propto 1/\sqrt{C_{\mathrm{H2SO4}}}$. Even if the Gouy-Chapman-Stern model does not strictly apply to our experimental conditions, we still expect a strong dependence of κ on the concentration C_{H2SO4} of the supporting electrolyte, because the latter determines the width of the diffuse layer, and thus the distribution of the electrostatic potential drop across the interface.

To test this effect, we measured the 10 mM Ce(IV) reduction on Au_{poly} also in 0.5 M H_2SO_4 and in 2 M H_2SO_4, and we fitted the transfer coefficients $\alpha_{cathodic}$ as before. We obtained $\alpha_{cathodic}^{0.5\ \mathrm{M\ H2SO4}} = 0.138 \pm 0.004$ and $\alpha_{cathodic}^{2\ \mathrm{M\ H2SO4}} = 0.153 \pm 0.002$, respectively, to be compared with our previous value $\alpha_{cathodic}^{1\ \mathrm{M\ H2SO4}} = 0.154 \pm 0.001$ obtained in 1 M H_2SO_4. In relation to the variations in C_{H2SO4}, these changes in $\alpha_{cathodic}$ are negligible. The transfer coefficient is largely independent of the sulfuric acid concentration, in contradiction to our expectation based on the Frumkin effect.

Electrochemical dissociation field effect

In the Frumkin-Marcus-Hush model the concentration of cerium complexes at the PCA is in equilibrium with the bulk electrolyte, whereas the rate-determining step is the electron transfer between electrode and cerium complexes across the inner (Stern) layer. To resolve the issue with an unphysically large fitted value of κ obtained from the Frumkin-Marcus-Hush model, we seek for an alternative mechanism where the rate-determining step lies beyond the PCA in the diffuse (outer) layer. We propose the *field-enhanced dissociation of cerium–sulfate complexes*, similar to the second Wien effect, as the rate-determining step of the electrochemical Ce(III)/Ce(IV) redox mechanism on Au electrodes in sulfuric acid, as

discussed in the following. Similar electrochemical dissociation field effects in the diffuse layer were already discussed in a different context[81, 82].

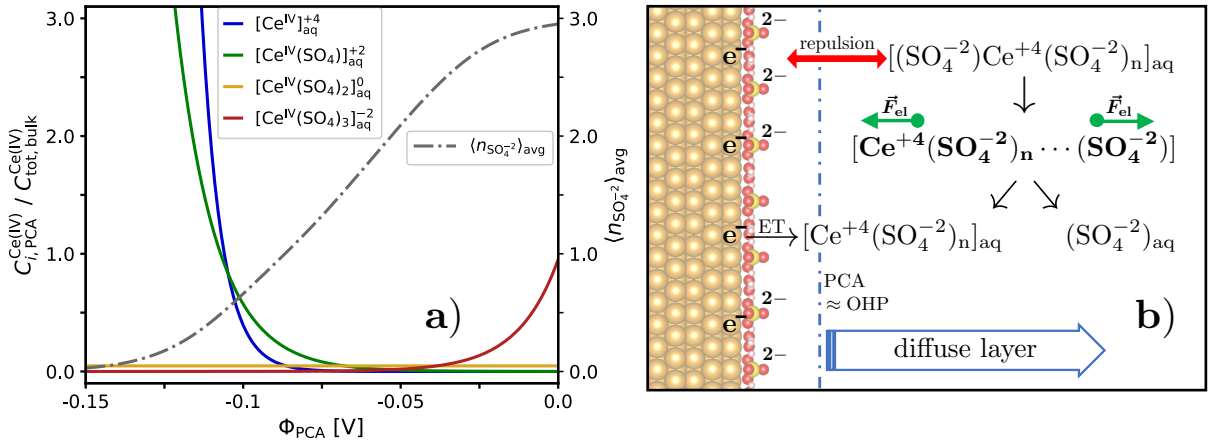

Fig. 5: (a) Calculated equilibrium concentrations of Ce(IV)–sulfate complexes, relative to the total bulk concentration, at the PCA (left axis) and average number of sulfate ligands per Ce(IV) (right axis) as a function of the local potential at the PCA. (b) Schematic of the field-enhanced dissociation of Ce(IV)–sulfate complexes in the diffuse part of the electrochemical double-layer. The Au electrode surface is covered with sulfate adsorbates, formally indicated with a charge of $-2e$, and, due to its high PZC, the electrode additionally carries a negative electronic surface charge, both of which contribute to the repulsion of the sulfate ligands of the cerium complexes.

Fig. 5a shows the equilibrium concentrations of the different Ce(IV)–sulfate complexes at the PCA, computed from Equation (11), as a function of the local potential Φ_{PCA}. The concentrations are normalized w.r.t. the total Ce(IV) concentration in the bulk electrolyte. For $\Phi_{\mathrm{PCA}} = 0$, the relative concentrations at the PCA are equal to the bulk values, cf. Supporting Information Fig. S1. As discussed above, our experimental potential range is strongly on the negative side from the PZC of the sulfate-covered Au electrode surface. From Equation (9), together with our computed range of values for the PZC and $\Phi^0_{\mathrm{PCA}} \leq 0$ due to the negatively charged sulfate adsorbates, it appears realistic to assume that Φ_{PCA} lies around -0.1 to -0.15 V in our experimental potential range, even for a small value of κ around 0.1. As a result, the concentration of the tri- and di-sulfate complexes, which dominate in the bulk electrolyte, becomes negligible at the PCA in comparison to the positively charged mono- and zero-sulfate complexes. This is the effect of the repulsion between the negatively charged electrode surface and the sulfate ligands of the cerium complexes. In addition, the sulfate adsorbates on the Au surface will amplify the repulsive interaction with the sulfate ligands. Accordingly, the average number of sulfate ligands per Ce(IV) drops from its bulk value close to three down to almost zero for $\Phi_{\mathrm{PCA}} = -0.15$ V, as shown in Fig. 5a. Thus, to overcome the repulsive interaction, the Ce(IV) must lose a large fraction of their sulfate ligands when crossing the diffuse part of the electrochemical double-layer in order to reach the PCA. We therefore propose the hypothesis that the cerium–sulfate complex dissociation in the diffuse layer,

$$[\mathrm{Ce}^{+4}(\mathrm{SO}_4^{-2})_{n+1}]_{\mathrm{aq}} \longrightarrow [\mathrm{Ce}^{+4}(\mathrm{SO}_4^{-2})_n]_{\mathrm{aq}} + (\mathrm{SO}_4^{-2})_{\mathrm{aq}} \qquad \text{(Reaction 4)}$$

is the rate-determining step for the electrochemical Ce(IV) reduction in sulfuric acid on a gold electrode, as shown schematically in Fig. 5b. The dissociation step (Reaction 4) is assisted by the electrostatic field $\vec{E}_{\mathrm{el}}$ across the diffuse layer, which produces electrostatic forces $\vec{F}_{\mathrm{el}}$ that pull the complex apart and split off a sulfate ligand. The remaining complex carries a doubly more positive charge, allowing it to approach the negatively charged electrode surface and being available for electron transfer (ET). The rate-limiting complex dissociation breaks the thermodynamic equilibrium between the concentrations in the bulk electrolyte and at the PCA. Instead, the cerium concentrations at the PCA follow a Nernst equilibrium due to the fast electron transfer.

The proposed mechanism consistently explains our experimental results. To describe the field effect mathematically, we first approximate the electrostatic field by the difference quotient $\left|\vec{E}_{\mathrm{el}}\right| \approx |\Phi_{\mathrm{PCA}}|/\lambda_{\mathrm{D}}$, because Φ_{PCA} is equal to the potential drop across the diffuse layer with a width characterized by the Debye length λ_{D}. We then heuristically assume that the dependence of the dissociation rate on the electrostatic field can be described by a Boltzmann factor

$$R_{\mathrm{diss}} \;=\; R^{0}_{\mathrm{diss}} \exp\left(\frac{\nu q|\vec{E}_{\mathrm{el}}|}{kT}\right) \;\propto\; \exp\left(\frac{\nu q \kappa}{\lambda_{\mathrm{D}} kT}\,|E - E_{\mathrm{PZC}}|\right) \qquad (14)$$

where we used Equation (9), and where R^{0}_{diss} is the dissociation rate at zero field strength, $q = 2e$ is the magnitude of the charge separated in the dissociation step, and ν is a parameter with the dimension of a length that characterizes how far the complex must be stretched by the electrostatic field to reach the transition state for dissociation. A more detailed motivation for the form (14) is given in the Supporting Information, together with a short discussion of its relation to the Onsager theory[83] for the second Wien effect. From Equation (14) we obtain a transfer coefficient

$$\alpha_{\mathrm{diss}} \;=\; -(kT/e)\frac{\partial}{\partial E}\ln(R_{\mathrm{diss}}) \;=(q/e)\,\kappa\frac{\nu}{\lambda_{\mathrm{D}}} \;=\; 2\kappa\frac{\nu}{\lambda_{\mathrm{D}}} \qquad (15)$$

which would be equal to our experimentally determined transfer coefficient $\alpha_{cathodic} = 0.157$. As argued in the Supporting Information, we expect $\nu \leq \lambda_{\mathrm{D}}$, so we obtain $\kappa \geq 0.08$ in reasonable agreement with electrochemical double-layer theory. Furthermore, Equation (15) can explain the observed insensitivity of the transfer coefficient towards the sulfuric acid concentration. As discussed above, κ is expected to be approximately proportional to λ_{D}, so changes in λ_{D} resulting from changes in the sulfuric acid concentration get cancelled in Equation (15). Our experimental results thus provide strong evidence for the proposed mechanism.

Finally, the Nernst equilibrium at the PCA guarantees that the cathodic and anodic transfer coefficients, measured separately for the Ce(IV) reduction and Ce(III) oxidation, respectively,

precisely add up to one. This holds in general when the rate-determining complex dissociation and recombination across the diffuse layer is first-order-dependent on the respective reactant concentrations, as discussed in detail in the Supporting Information. In short, it can be shown that for arbitrary bulk concentrations C_R^B and C_O^B of Ce(III) and Ce(IV), respectively, the total kinetic current can be written $I_{kin}(E) = C_R^B F A k_{\mathrm{ox}}(E) - C_O^B F A k_{\mathrm{red}}(E)$, which is the superposition of oxidation and reduction branches $I_{\mathrm{ox}}(E) = C_R^B F A k_{\mathrm{ox}}(E)$ and $I_{\mathrm{red}}(E) = -C_O^B F A k_{\mathrm{red}}(E)$ with potential-dependent effective rate constants $k_{\mathrm{ox}}(E)$ and $k_{\mathrm{red}}(E)$. Note that both branches have a first-order dependence on the bulk concentration of the respective reactant species. In our experimental potential range, where E is significantly negative of E^0, the effective rate constant of the reduction reaction $k_{\mathrm{red}}(E)$ is essentially equal to the rate constant of the Ce(IV)–sulfate complex dissociation step. For any electrode potential E, we are free to consider bulk concentrations that fulfill the global Nernst equation $E = E^0 + (RT/F)\ln\left(C_O^{\mathrm{eq}}/C_R^{\mathrm{eq}}\right)$. The corresponding global equilibrium requires $I_{kin}(E) = 0$, from which $\alpha_{cathodic} + \alpha_{anodic} = 1$ directly follows, using the general definitions $\alpha_{cathodic} = -(RT/F)\frac{\partial}{\partial E}\ln(|I_{\mathrm{red}}(E)|)$ and $\alpha_{anodic} = (RT/F)\frac{\partial}{\partial E}\ln(I_{\mathrm{ox}}(E))$. The derivation is presented in detail in the Supporting Information.

As expressed in Equation (14) the dissociation field effect in the outer electrochemical double-layer is controlled by the potential of zero charge of the electrode, which is determined by the electronic structure, in particular the work function, of the electrode material and surface. We therefore regard it as an effect that is susceptible to electrocatalysis. However, unlike typical electrocatalytic mechanisms that proceed within the inner layer involving surface adsorbate intermediates, the present mechanism would be an example of electrocatalysis acting in the outer layer, mediated by the electrostatic field. A further demonstration of the electrocatalytic aspect is given in the following section.

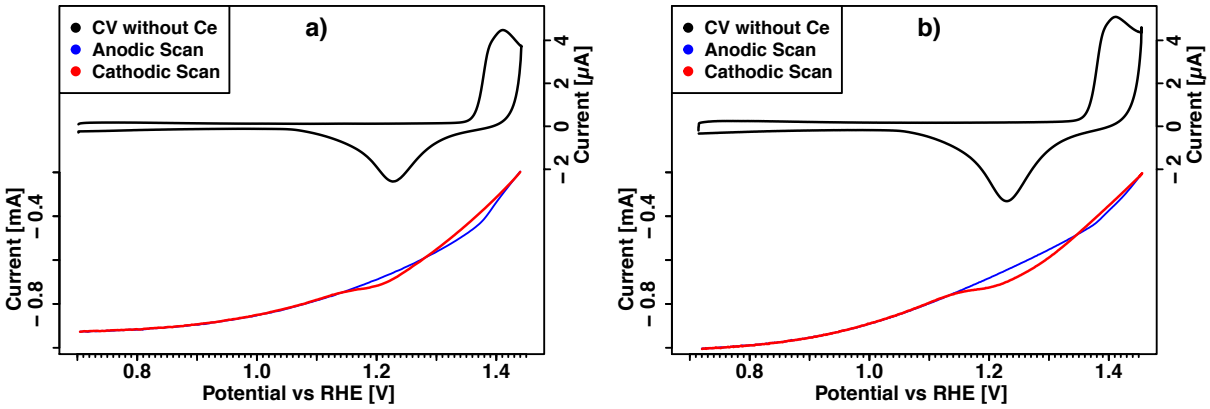

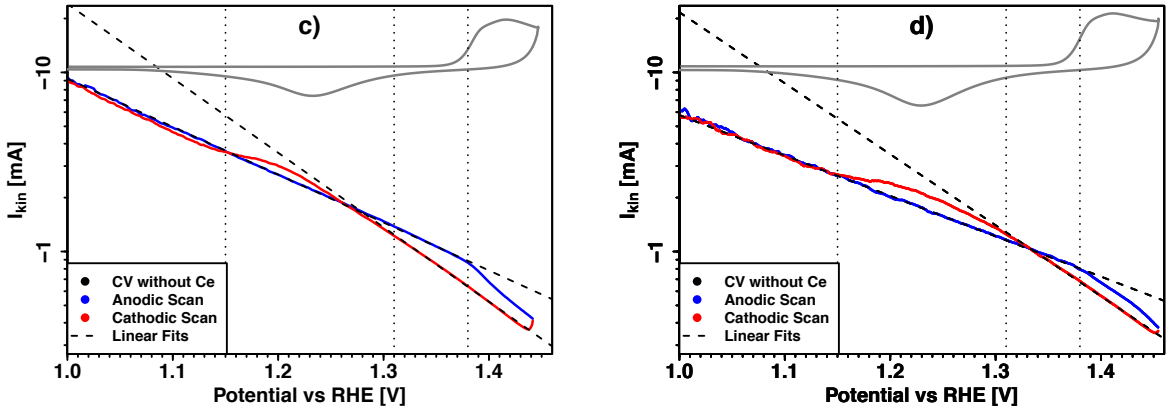

Fig. 6: RDE curves (a) and (b) at 2500 rpm and 10 mV/s, and Tafel plots (c) and (d) of the corresponding kinetic currents obtained for 10 mM Ce(IV) in 1 M H_2SO_4 (a,c) and 0.5 M H_2SO_4 (b,d) electrolyte solutions, respectively, as well as the corresponding Au_{poly} CVs without Ce species in solution.

Kinetic enhancement on an oxidized Au surface

We investigated the influence of gold surface oxidation on the Ce(IV) reduction kinetics. The oxidation of the gold surface starts in the positive-going scan at 1.35 V_{RHE} with a sharp increase at 1.38 V_{RHE}, cf. Fig. 2. The formed surface oxide layer is reduced in the negative-going scan between 1.35 V_{RHE} and 1.05 V_{RHE}. Figs. 6a,b show typical RDE curves obtained for 10 mM Ce(IV) in 1 M and 0.5 M sulfuric acid electrolyte, respectively. The Ce(IV) reduction kinetics became slower with the onset of gold surface oxidation in the positive-going scan. Most surprisingly however, during reduction of the gold surface in the negative-going scan, the overall cathodic currents temporarily surpassed the corresponding currents of the positive-going scan. This enhancement of the Ce(IV) reduction kinetics was stronger in the 0.5 M sulfuric acid electrolyte. Insufficient correction of gold reduction currents can be excluded as explanation, because the RDE currents were already corrected for the Au_{poly} CV currents. In addition, the observed difference in currents between positive-going and negative-going scan is one order of magnitude larger than the currents resulting from gold surface reduction alone, cf. Fig. 6.

The Tafel plots in Figs. 6c,d demonstrate that, in fact, the observed correlation between the kinetic enhancement and the Au surface reduction process is only apparent, but not directly causal. The kinetic currents of the Ce(IV) reduction on the oxidized Au surface in the first part of the negative-going scan reveal a very linear Tafel plot that is characterized by a smaller value of the rate constant, but a steeper slope, i.e. transfer coefficient, than the kinetics on the reduced Au surface. From linear fits in the potential range 1.35 – 1.40 V_{RHE} of the negative-going scans, we obtained $k_0^{\mathrm{AuOx}} = (2.2 \pm 0.3) \times 10^{-3}$ cm/s and $\alpha_{cathodic}^{\mathrm{AuOx}} = 0.24 \pm 0.01$ for the reduction kinetics of 10 mM Ce(IV) in 1 M H_2SO_4. Because of the different slopes and only a minor decrease of the rate constant, there exists a crossing point between the Ce(IV) reduction kinetics on the oxidized and reduced Au surface, respectively, which becomes visible as a result of the hysteresis between Au oxidation and reduction in the positive-going vs. negative-going scans. In the potential range negative of the crossing point, the kinetics on the oxidized Au surface are faster than on the reduced surface. This is a surprising example how

electrode surface oxidation can have a positive electrocatalytic effect on the electrochemical redox kinetics of dissolved cation complexes.

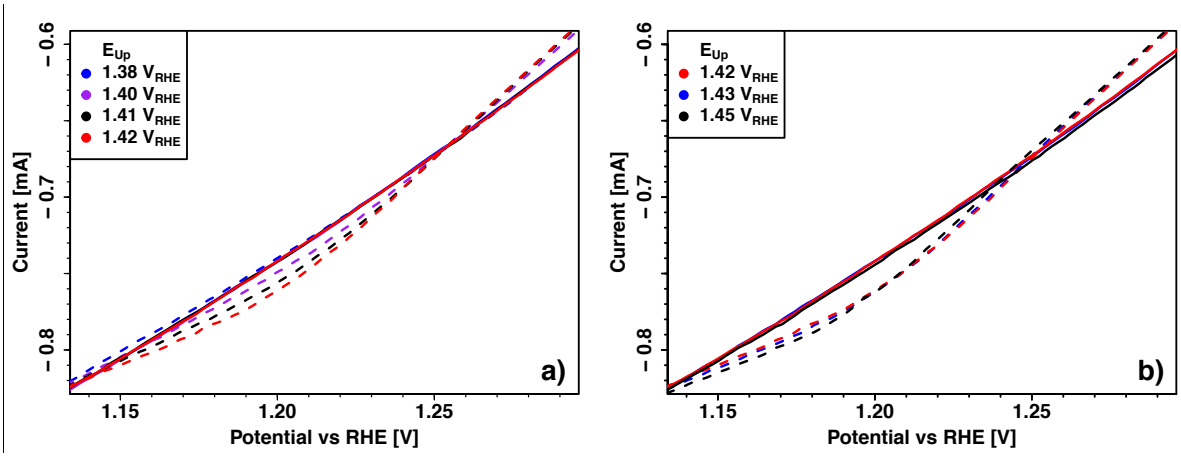

Fig. 7: Potential region of the kinetic enhancement of the Ce(IV) reduction reaction for different upper potential limits (vs. RHE). Positive-going sweeps (solid lines) and negative-going sweeps (dashed lines). 10 mM Ce(IV) in 1 M H_2SO_4, 20 mV/s, 2500 rpm.

Fig. 7 shows the kinetic enhancement as a function of the upper potential limit, which determines the oxide-coverage of the gold surface. The kinetic enhancement was not observable for upper potential limits below (and including) 1.38 V_{RHE}, and it increased with increasing upper limit until 1.42 V_{RHE}, cf. Fig. 7a. Further increase of the upper potential limit did not further increase the kinetic enhancement, cf. Fig. 7b. Because Au oxidation already starts around 1.35 V_{RHE}, these results show firstly that a minimum oxide coverage is necessary to trigger the effect, and secondly that it saturates after a certain oxide coverage is reached.

The observed effects of Au surface oxidation on the Ce(IV) reduction kinetics can be explained by the same dissociation field effect as proposed above for the mechanism on the reduced, sulfate-covered Au surface. With the onset of Au surface oxidation, the sulfate-adsorbate layer, present in the flat region of the CV, cf. Fig. 2, gets replaced by a surface oxide layer. As a result, the potential of zero charge shifts from that of the sulfate-covered Au surface to the PZC of the oxidized Au surface. To estimate the latter, we performed DFT calculations for various Au(111) surface oxide layers. Within the upper potential limits of our experiments, we can neglect the formation of sub-surface oxides[84] and focus on surface-adsorbed oxygen species. The relevant relaxed structures are given in the Supporting Information. In agreement with recent reports[37], we found that Au(111) surface oxidation directly starts with O-adsorption, which is more stable than OH-adsorption. To form a (1/4)-coverage of O_{ads} on the Au(111) surface, we computed an equilibrium potential of 1.28 V_{SHE} (without including the influence of the sulfate adsorbates present on the reduced surface). Although our experiments were performed with a polycrystalline Au electrode, the agreement between the computed potential and our experimentally determined potential for gold surface oxidation is very good. The computed PZC values for the (1/4) and (1/2)-coverages of O_{ads} on the Au(111)

surface are given in Table 4. To estimate the oxide coverage reached in our experiments, we determined a total Au oxidation charge of 184 µC/cm^2 for the upper potential limit of 1.44 V_{RHE} from our Au_{poly} CV in 1 M H_2SO_4, see Fig. 2. For the Au(111) surface, this would correspond to roughly 0.8 electrons per surface Au atom, which is approximately equivalent to 0.4 O_{ads}. However, as discussed above, the Au(111) surface is covered with 0.2 $(SO_4)_{ads}$ at the onset of surface oxidation. Because both adsorbates carry a formal charge of $-2e$, the current contributions of the replacement of the 0.2 $(SO_4)_{ads}$ by 0.2 O_{ads} should approximately cancel. Adding these "silent" 0.2 O_{ads}, we obtain a total estimate of 0.6 for the O_{ads}-coverage reached in our experiments, which is close to the (1/2)-coverage considered in our DFT calculations. For this, we computed a PZC of $1.45\ \mathrm{V_{SHE}}$, which is close to our experimental potential range. Consequently, the electrochemical double-layer is less charged for the oxidized Au surface than for the reduced, sulfate-covered surface. The weaker electrostatic fields result in a reduced dissociation rate according to Equation (14) in agreement with the lower value of the kinetic rate constant k_0^{AuOx}. However, according to electrochemical double-layer theory, the fraction κ of the potential drop across the outer layer is larger close to the PZC. Together with Equation (15), this explains the larger value of the transfer coefficient $\alpha_{cathodic}^{\mathrm{AuOx}} = 0.24$, from which we estimate $\kappa \geq 0.12$. The electrochemical dissociation field effect can thus provide a consistent description of the kinetics on both the reduced and the oxidized Au surface.

Conclusion

Using an experimental approach to separately investigate the kinetics of the electrochemical Ce(III) oxidation and Ce(IV) reduction within the identical potential range, we discovered that their respective kinetic currents in 1 M H_2SO_4 on a reduced Au_{poly} surface were perfectly described by the Butler-Volmer equation with an exceptional asymmetry: We determined anodic and cathodic transfer coefficients of $\alpha_{anodic} = 0.84 \pm 0.02$ and $\alpha_{cathodic} = 0.157 \pm 0.006$, respectively, which exactly add up to one as required. To further explore the possible origin of this intriguing asymmetry, we tested different flavors of Marcus theory to fit our experimental data, but none of the models was able to reproduce the perfectly linear Tafel plot of the experimental data with physically reasonable parameter values. Based on the Frumkin effect, we extended our analysis and demonstrated that the majority of cerium–sulfate complexes are repelled from the electrode surface in our experimental potential range. We consequently proposed the field-enhanced dissociation of cerium–sulfate complexes as the rate-determining step of the Ce(IV) reduction kinetics. The same mechanism provides an explanation for the enhancement of the Ce(IV) reduction kinetics observed on an electrochemically oxidized gold surface in a certain potential range. The dependence of the dissociation field effect on the potential of zero charge demonstrates how electrochemical processes in the outer part of the electrochemical double-layer can be controlled by electrode material- and surface-specific properties. Our findings show how the redox kinetics of dissolved species can be susceptible to electrocatalytic tuning, and they reveal that the electrochemical Ce(III)/Ce(IV) redox couple on gold electrodes is a highly intriguing case for further theoretical and experimental studies.

Supporting Information

Calculation of concentrations and free energies of cerium–sulfate complexes; Discussion of Marcus theory models for electrochemical outer-sphere electron transfer and data fitting procedure; Derivation of GAMH model equations; Motivation of the mathematical form used for the analysis of the electrochemical dissociation field effect; Rate equations and sum of transfer coefficients; Relaxed structures from the DFT computations of Au(111) surfaces with different adsorbates.

Acknowledgements

Innosuisse and the Swiss Competence Center for Energy Research (SCCER) Heat & Electricity Storage is acknowledged. T.B. acknowledges financial support in the form of research fellowship grant No. P400P2_186671 funded by the SNSF (Swiss National Science Foundation).

References

1. Arenas, L. F.; de Leon, C. P.; Walsh, F. C., Electrochemical redox processes involving soluble cerium species. *Electrochim. Acta* **2016,** *205*, 226-247.
2. Varela, J. A.; Oberg, S. G.; Neustedter, T. M.; Nelson, N., Non-thermal organic waste destruction: Characterization of the CerOx system 4. *Environ. Prog.* **2001,** *20* (4), 261-271.
3. Binnemans, K., Applications of Tetravalent Cerium Compounds. *Hbk Phys. Chem. Rare* **2006,** *36*, 281-392.
4. Harrison, S.; Theoret, A., The electrosynthesis of naphthoquinone, and tetrahydroanthraquinone. *J. New Mat. Elect. Syst.* **1999,** *2* (1), 1-9.
5. Nzikou, J. M.; Aurousseau, M.; Lapicque, F., Electrochemical Investigations of the Ce(III)/Ce(IV) Couple Related to a Ce(Iv)-Assisted Process for SO2/NOx, Abatement. *J. Appl. Electrochem.* **1995,** *25* (10), 967-972.
6. Pillai, K. C.; Raju, T.; Chung, S. J.; Moon, I. S., Removal of H2S using a new Ce(IV) redox mediator by a mediated electrochemical oxidation process. *J. Chem. Technol. Biot.* **2009,** *84* (3), 447-453.
7. Liu, Y.; Xia, X.; Liu, H., Studies on cerium (Ce4+/Ce3+)-vanadium(V2+/V3+) redox flow cell-cyclic voltammogram response of Ce4+/Ce3+ redox couple in H2SO4 solution. *J. Power Sources* **2004,** *130* (1-2), 299-305.
8. Walsh, F. C.; de Leon, C. P.; Berlouis, L.; Nikiforidis, G.; Arenas-Martinez, L. F.; Hodgson, D.; Hall, D., The Development of Zn-Ce Hybrid Redox Flow Batteries for Energy Storage and Their Continuing Challenges. *ChemPlusChem* **2015,** *80* (2), 288-311.
9. Xia, X.; Liu, H. T.; Liu, Y., Studies on Ce4+ /Ce3+ redox system using linear polarization and ac impedance techniques. *Acta Chim. Sinica* **2002,** *60* (9), 1630-1636.
10. Xie, Z. P.; Liu, Q. C.; Chang, Z. W.; Zhang, X. B., The developments and challenges of cerium half-cell in zinc-cerium redox flow battery for energy storage. *Electrochim. Acta* **2013,** *90*, 695-704.
11. Nikiforidis, G.; Daoud, W. A., Effect of Mixed Acid Media on the Positive Side of the Hybrid Zinc-Cerium Redox Flow Battery. *Electrochim Acta* **2014,** *141*, 255-262.
12. Piwek, J.; Dennison, C. R.; Frackowiak, E.; Girault, H.; Battistel, A., Vanadium-oxygen cell for positive electrolyte discharge in dual-circuit vanadium redox flow battery. *J. Power Sources* **2019,** *439*, 227075.
13. Bishop, E.; Cofre, P., Anodic Generation of Cerium(IV) - Charge-Transfer Kinetic-Parameters and Conditional Potentials at Platinum, Gold and Glassy-Carbon. *Analyst* **1981,** *106* (1260), 316-322.
14. Bonewitz, R. A.; Schmid, G. M., Oxygen Adsorption on Gold and Ce(III)/Ce(IV) Reaction. *J. Electrochem. Soc.* **1970,** *117* (11), 1367-1372.

15. Kiekens, P.; Steen, L.; Donche, H.; Temmerman, E., Kinetics of Ce(IV) Reduction at Gold, Carbon and Iridium Electrodes. *Electrochim. Acta* **1981,** *26* (7), 841-845.
16. Sacchetto, G. A.; Pastore, P.; Favaro, G.; Fiorani, M., Liquid-Chromatographic Determination of Nonvolatile Nitrosamines by Postcolumn Redox Reactions and Voltammetric Detection at Solid Electrodes - Behavior of the Ce(IV)-Ce(III) Couple at Gold, Platinum and Glassy-Carbon Electrodes and Suitability of the Ce(IV) Reagent. *Anal. Chim. Acta* **1992,** *258* (1), 99-108.
17. Modiba, P.; Crouch, A. M., Electrochemical study of cerium(IV) in the presence of ethylenediaminetetraacetic acid (EDTA) and diethylenetriaminepentaacetate (DTPA) ligands. *J. Appl. Electrochem.* **2008,** *38* (9), 1293-1299.
18. Randle, T. H.; Kuhn, A. T., Kinetics and Mechanism of the Cerium(IV) Cerium(III) Redox Reaction on a Platinum-Electrode. *J. Chem. Soc. Farad. T 1* **1983,** *79*, 1741-1756.
19. Xie, Z. P.; Xiong, F. J.; Zhou, D. B., Study of the Ce3+/Ce4+ Redox Couple in Mixed-Acid Media (CH3SO3H and H2SO4) for Redox Flow Battery Application. *Energ. Fuel* **2011,** *25* (5), 2399-2404.
20. Xiong, F. J.; Zhou, D. B.; Xie, Z. P.; Chen, Y. Y., A study of the Ce3+/Ce4+ redox couple in sulfamic acid for redox battery application. *Appl. Energ.* **2012,** *99*, 291-296.
21. Henning, S.; Herranz, J.; Gasteiger, H. A., Bulk-Palladium and Palladium-on-Gold Electrocatalysts for the Oxidation of Hydrogen in Alkaline Electrolyte. *J. Electrochem. Soc.* **2015,** *162* (1), F178-F189.
22. Bard, A. J., Faulkner, Larry R., *Electrochemical Methods: Fundamentals and Applications*. 2 ed.; Wiley & Sons Ltd: New York, 2010; p 864.
23. Guidelli, R.; Compton, R. G.; Feliu, J. M.; Gileadi, E.; Lipkowski, J.; Schmickler, W.; Trasatti, S., Definition of the transfer coefficient in electrochemistry (IUPAC Recommendations 2014). *Pure Appl. Chem.* **2014,** *86* (2), 259-262.
24. Guidelli, R.; Compton, R. G.; Feliu, J. M.; Gileadi, E.; Lipkowski, J.; Schmickler, W.; Trasatti, S., Defining the transfer coefficient in electrochemistry: An assessment (IUPAC Technical Report). *Pure Appl. Chem.* **2014,** *86* (2), 245-258.
25. Kresse, G.; Furthmuller, J., Efficiency of ab-initio total energy calculations for metals and semiconductors using a plane-wave basis set. *Comp. Mater. Sci.* **1996,** *6* (1), 15-50.
26. Kresse, G.; Joubert, D., From ultrasoft pseudopotentials to the projector augmented-wave method. *Phys. Rev. B* **1999,** *59* (3), 1758-1775.
27. Perdew, J. P.; Burke, K.; Ernzerhof, M., Generalized gradient approximation made simple (vol 77, pg 3865, 1996). *Phys. Rev. Lett.* **1997,** *78* (7), 1396-1396.
28. Grimme, S.; Antony, J.; Ehrlich, S.; Krieg, H., A consistent and accurate ab initio parametrization of density functional dispersion correction (DFT-D) for the 94 elements H-Pu. *J. Chem. Phys.* **2010,** *132* (15), 154104

29. Grimme, S.; Ehrlich, S.; Goerigk, L., Effect of the Damping Function in Dispersion Corrected Density Functional Theory. *J. Comput. Chem.* **2011,** *32* (7), 1456-1465.
30. Ong, S. P.; Richards, W. D.; Jain, A.; Hautier, G.; Kocher, M.; Cholia, S.; Gunter, D.; Chevrier, V. L.; Persson, K. A.; Ceder, G., Python Materials Genomics (pymatgen): A robust, open-source python library for materials analysis. *Comp. Mater. Sci.* **2013,** *68*, 314-319.
31. Ataka, K.; Osawa, M., In situ infrared study of water-sulfate coadsorption on gold(111) in sulfuric acid solutions. *Langmuir* **1998,** *14* (4), 951-959.
32. Cuesta, A.; Kleinert, M.; Kolb, D. M., The adsorption of sulfate and phosphate on Au(111) and Au(100) electrodes: an in situ STM study. *Phys. Chem. Chem. Phys.* **2000,** *2* (24), 5684-5690.
33. Edens, G. J.; Gao, X. P.; Weaver, M. J., The Adsorption of Sulfate on Gold(111) in Acidic Aqueous-Media - Adlayer Structural Inferences from Infrared-Spectroscopy and Scanning-Tunneling-Microscopy. *J. Electroanal. Chem.* **1994,** *375* (1-2), 357-366.
34. Magnussen, O. M.; Hagebock, J.; Hotlos, J.; Behm, R. J., In-Situ Scanning-Tunneling-Microscopy Observations of a Disorder-Order Phase-Transition in Hydrogensulfate Adlayers on Au(111). *Faraday Discuss.* **1992,** *94*, 329-338.

35. Fang, Y.; Ding, S. Y.; Zhang, M.; Steinmann, S. N.; Hu, R.; Mao, B. W.; Feliu, J. M.; Tian, Z. Q., Revisiting the Atomistic Structures at the Interface of Au(111) Electrode-Sulfuric Acid Solution. *J. Am. Chem. Soc.* **2020,** *142* (20), 9439-9446.
36. Gossenberger, F.; Juarez, F.; Gross, A., Sulfate, Bisulfate, and Hydrogen Co-adsorption on Pt(111) and Au(111) in an Electrochemical Environment. *Front. Chem.* **2020,** *8*, 634.
37. Pfisterer, J. H. K.; Nattino, F.; Zhumaev, U. E.; Breiner, M.; Feliu, J. M.; Marzari, N.; Domke, K. F., Role of OH Intermediates during the Au Oxide Electro-Reduction at Low pH Elucidated by Electrochemical Surface-Enhanced Raman Spectroscopy and Implicit Solvent Density Functional Theory. *ACS Catal.* **2020,** *10* (21), 12716-12726.
38. Mathew, K.; Sundararaman, R.; Letchworth-Weaver, K.; Arias, T. A.; Hennig, R. G., Implicit solvation model for density-functional study of nanocrystal surfaces and reaction pathways. *J. Chem. Phys.* **2014,** *140* (8), 084106.
39. Filhol, J. S.; Neurock, M., Elucidation of the electrochemical activation of water over Pd by first principles. *Angew. Chem. Int. Edit.* **2006,** *45* (3), 402-406.
40. Norskov, J. K.; Rossmeisl, J.; Logadottir, A.; Lindqvist, L.; Kitchin, J. R.; Bligaard, T.; Jonsson, H., Origin of the overpotential for oxygen reduction at a fuel-cell cathode. *J. Phys. Chem. B* **2004,** *108* (46), 17886-17892.
41. Linstrom, P. J.; Mallard, W. G., *NIST Standard Reference Database Number 69*. National Institute of Standards and Technology: Gaithersburg MD, 2018.
42. Cox, J. D.; Wagman, D. D.; Medvedev, V. A., *CODATA Key Values for Thermodynamics*. Hemisphere Publishing Corp.: New York, 1989.
43. Paulenova, A.; Creager, S. E.; Navratil, J. D.; Wei, Y., Redox potentials and kinetics of the Ce3+/Ce4+ redox reaction and solubility of cerium sulfates in sulfuric acid solutions. *J. Power Sources* **2002,** *109* (2), 431-438.
44. Wadsworth, E.; Duke, F. R.; Goetz, C. A., Present Status of Cerium(IV)-Cerium(III) Potentials. *Anal. Chem.* **1957,** *29* (12), 1824-1825.
45. Bauer, H. H., Electrochemical Transfer-Coefficient. *J. Electroanal. Chem.* **1968,** *16* (3), 419-432.
46. Bockris, J. O.; Nagy, Z., Symmetry Factor and Transfer Coefficient - Source of Confusion in Electrode Kinetics. *J. Chem. Educ.* **1973,** *50* (12), 839-843.
47. Khan, S. U. M.; Bockris, J. O., Electronic States in Solution and Charge-Transfer. *J. Phys. Chem.* **1983,** *87* (14), 2599-2603.
48. Gileadi, E., *Physical Electrochemistry: Fundamentals, Techniques and Applications*. 1 ed.; Wiley-VCH: Weinheim, Germany, 2011; p 68.
49. Gileadi, E.; Kirowa-Eisner, E., Some observations concerning the Tafel equation and its relevance to charge transfer in corrosion. *Corros. Sci.* **2005,** *47* (12), 3068-3085.
50. Petrii, O. A.; Nazmutdinov, R. R.; Bronshtein, M. D.; Tsirlina, G. A., Life of the Tafel equation: Current understanding and prospects for the second century. *Electrochim. Acta* **2007,** *52* (11), 3493-3504.
51. Marcus, R. A., On the Theory of Oxidation-Reduction Reactions Involving Electron Transfer .1. *J. Chem. Phys.* **1956,** *24* (5), 966-978.
52. Marcus, R. A., Electrostatic Free Energy and Other Properties of States Having Nonequilibrium Polarization .1. *J. Chem. Phys.* **1956,** *24* (5), 979-989.
53. Marcus, R. A., Theory of Oxidation-Reduction Reactions Involving Electron Transfer .2. Applications to Data on the Rates of Isotopic Exchange Reactions. *J. Chem. Phys.* **1957,** *26* (4), 867-871.
54. Marcus, R. A., On Theory of Electron-Transfer Reactions .6. Unified Treatment for Homogeneous and Electrode Reactions. *J. Chem. Phys.* **1965,** *43* (2), 679-701.
55. Marcus, R. A., Electron-Transfer Reactions in Chemistry - Theory and Experiment. *Rev. Mod. Phys.* **1993,** *65* (3), 599-610.
56. Blatz, L. A., Use of a Cation-Exchange Resin to Study Cerous and Sulfate Ion Complexes. *J. Phys. Chem.* **1962,** *66* (1), 160-164.

57. Decarvalho, R. G.; Choppin, G. R., Lanthanide and Actinide Sulfate Complexes .2. Determination of Thermodynamic Parameters. *J. Inorg. Nucl. Chem.* **1967,** *29* (3), 737-743.
58. Hardwick, T. J.; Robertson, E., Association of Ceric Ions with Sulphate (a Spectral Study). *Can. J. Chem.* **1951,** *29* (10), 828-837.
59. Chidsey, C. E. D., Free-Energy and Temperature-Dependence of Electron-Transfer at the Metal-Electrolyte Interface. *Science* **1991,** *251* (4996), 919-922.
60. Hush, N. S., Adiabatic Rate Processes at Electrodes .1. Energy-Charge Relationships. *J. Chem. Phys.* **1958,** *28* (5), 962-972.
61. Hush, N. S., Electron transfer in retrospect and prospect 1: Adiabatic electrode processes (vol 460, p 5, 1999). *J. Electroanal. Chem.* **1999,** *470* (2), 170-195.
62. Laborda, E.; Henstridge, M. C.; Batchelor-McAuley, C.; Compton, R. G., Asymmetric Marcus-Hush theory for voltammetry. *Chem. Soc. Rev.* **2013,** *42* (12), 4894-4905.
63. Laborda, E.; Henstridge, M. C.; Compton, R. G., Asymmetric Marcus theory: Application to electrode kinetics. *J. Electroanal. Chem.* **2012,** *667*, 48-53.
64. Laborda, E.; Henstridge, M. C.; Compton, R. G., Giving physical insight into the Butler-Volmer model of electrode kinetics: Part 2-Nonlinear solvation effects on the voltammetry of heterogeneous electron transfer processes. *J. Electroanal. Chem.* **2012,** *681*, 96-102.
65. Hartnig, C.; Koper, M. T. M., Molecular dynamics simulations of solvent reorganization in electron-transfer reactions. *J. Chem. Phys.* **2001,** *115* (18), 8540-8546.
66. Biesheuvel, P. M.; van Soestbergen, M.; Bazant, M. Z., Imposed currents in galvanic cells. *Electrochim. Acta* **2009,** *54* (21), 4857-4871.
67. Dickinson, E. J. F.; Compton, R. G., Influence of the diffuse double layer on steady-state voltammetry. *J. Electroanal. Chem.* **2011,** *661* (1), 198-212.
68. Frumkin, A., Hydrogen overvoltage and the structure of the double layer. *Z. Phys. Chem. A-Chem T.* **1933,** *164* (1/2), 121-133.
69. Gavaghan, D. J.; Feldberg, S. W., Extended electron transfer and the Frumkin correction. *J. Electroanal. Chem.* **2000,** *491* (1-2), 103-110.
70. Timmer, B.; Sluyters.M; Sluyters, J. H., Electrode Kinetics and Double Layer Structure. *Surf. Sci.* **1969,** *18* (1), 44-61.
71. Hormann, N. G.; Andreussi, O.; Marzari, N., Grand canonical simulations of electrochemical interfaces in implicit solvation models. *J. Chem. Phys.* **2019,** *150* (4), 041730.
72. Kolb, D. M.; Schneider, J., Surface Reconstruction in Electrochemistry - Au(100)-(5x20), Au(111)-(1x23) and Au(110)-(1x2). *Electrochim. Acta* **1986,** *31* (8), 929-936.
73. Trasatti, S., Systematic Trends in the Crystal-Face Specificity of Interfacial Parameters - the Cases of Ag and Au. *J. Electroanal. Chem.* **1992,** *329* (1-2), 237-246.
74. Shi, Z.; Lipkowski, J.; Gamboa, M.; Zelenay, P.; Wieckowski, A., Investigations of SO4(2-) Adsorption at the Au(111) Electrode by Chronocoulometry and Radiochemistry. *J. Electroanal. Chem.* **1994,** *366* (1-2), 317-326.
75. McNaught, A. D.; Wilkinson, A., *IUPAC. Compendium of Chemical Terminology (the "Gold Book")*. 2nd ed.; Blackwell Scientific Publications: Oxford, 1997.
76. Alvarez, B.; Climent, V.; Feliu, J. M.; Aldaz, A., Determination of different local potentials of zero charge of a Pd-Au(111) heterogeneous surface. *Electrochem. Commun.* **2000,** *2* (6), 427-430.
77. Grahame, D. C., The Electrical Double Layer and the Theory of Electrocapillarity. *Chem. Rev.* **1947,** *41* (3), 441-501.
78. Stern, O., The theory of the electrolytic double shift. *Z. Elktrochem. Angew. P.* **1924,** *30*, 508-516.
79. Brown, M. A.; Abbas, Z.; Kleibert, A.; Green, R. G.; Goel, A.; May, S.; Squires, T. M., Determination of Surface Potential and Electrical Double-Layer Structure at the Aqueous Electrolyte-Nanoparticle Interface. *Phys. Rev. X* **2016,** *6* (1), 011007.
80. Schmickler, W., Electronic effects in the electric double layer. *Chem. Rev.* **1996,** *96* (8), 3177-3200.

81. Nürnberg, H. W., Influence of electric field in the double layer on rate constants determined with electrochemical relaxation techniques for fast homogeneous proton transfer reactions in solution. *Discussions of the Faraday Society* **1965,** *39*, 136-148.
82. Sanfeld, A.; Steinche.A, Association and Dissociation in Electrochemical Diffuse Layer. *T. Faraday Soc.* **1966,** *62* (523p), 1907-1914.
83. Onsager, L., Deviations from Ohm's Law in Weak Electrolytes. *J. Chem. Phys.* **1934,** *2* (9), 599-615.
84. Schneeweiss, M. A.; Kolb, D. M., Oxide formation on au(111) - An in situ STM study. *Solid State Ionics* **1997,** *94* (1-4), 171-179.